Paper No.
C2024-21225

AMPP ANNUAL CONFERENCE + EXPO
MARCH 3-7, 2024 | NEW ORLEANS, LOUISIANA

Implementation of Strong Acid and CO_2 Corrosion in CFD Software

Adam Cutright, Payman Sharifi, Srdjan Nesic, Bruce Brown
Institute for Corrosion and Multiphase Technology
342 West State Street
Athens, OH, 45701
United States

Muhammad Sami
Ansys
15915 Katy Fwy #550
Houston, TX, 77094
United States

ABSTRACT

To properly understand the necessary steps in implementing corrosion modeling into existing CFD software, it is necessary to verify the accuracy of the corrosion predictions made by the software. To do this, simulations are created that replicate experimental work performed in well understood geometries. The corrosion models are implemented in these simulations, and the resulting corrosion rates, as well as hydrodynamic and mass transfer characterizations, are compared to results from the experimental work. Presented herein is work investigating corrosion phenomena in a thin channel flow cell apparatus, as well as single phase straight pipe flow. In both geometries hydrodynamics, mass transfer, and electrochemistry have been simulated at a variety of conditions; the accuracy of the results were confirmed through comparison with experimental data and well tested correlations. Both geometries showed a high degree of agreement between the simulations and the experimental work, indicating that the methodology is viable to be used in other geometries.

Key words: Corrosion mechanisms, Corrosion rate, Oil and gas, Carbon dioxide, CFD

INTRODUCTION

In the oil and gas industry, use of models for prediction of corrosion to develop appropriate mitigation strategies is widespread. There are various models available for this purpose, one commonly used is MULTICORP™‡, which is a mechanistic corrosion prediction model. This is a 1-dimensional mechanistic model meaning it works by predicting corrosion at points along the length of a pipeline, making its predictions based on the actual corrosion mechanisms taking place as opposed to using empirical or semi-empirical models. 1-dimensional models rely on dimensionless number mass transfer correlations

‡ Trade Name

in order to predict pipe flow conditions which are used to make the corrosion predictions. These correlations are effective in laminar and turbulent, single phase, straight pipe flow.

Using a 1-dimensional system gives the advantage of having significantly fewer points at which calculations must be performed. It also avoids performing complex calculations to account for the flow values, instead replacing them with dimensionless number correlations. The downside to this approach is that in systems where these correlations do not currently exist, such as for many multiphase flow systems or when a more complex geometry is present (bends, valves, fittings, obstacles), these models cannot accurately predict corrosion.

To model corrosion in such systems, CFD (computational fluid dynamics) software can be implemented along with the appropriate understanding of the corrosion mechanisms. CFD software functions by taking a 2D or 3D geometry and breaking it down into a system of points at which flow variables and other system variables like temperature, pressure, species concentration will be calculated; this process is also known as discretization or meshing. Once the mesh has been created for the system the software then solves a number of equations simultaneously at each point inside the system using numerical methods. The equations solved will partly depend on what system variables are of interest to the user, those that must always be solved are the continuity equation, and the Navier-Stokes equation which are shown below.

$$\frac{\partial \rho}{\partial t} + \frac{\partial (\rho u_i)}{\partial x_i} = 0 \tag{1}$$

$$\frac{\partial \rho u_j}{\partial t} + \frac{\partial}{\partial x_i}\left(\rho u_j u_i\right) = \rho f_j - \frac{\partial P}{\partial x_j} + \frac{\partial}{\partial x_i}\left(\mu \frac{\partial u_j}{\partial x_i}\right) + \frac{1}{3}\frac{\partial}{\partial x_j}\left(\mu \frac{\partial u_i}{\partial x_i}\right) \tag{2}$$

In the case of a corrosion calculation the only thing left out in the above equations are the concentrations of species which are relevant to the corrosion reactions. These can be solved by including the species conservation equation which is shown below.

$$\frac{\partial}{\partial t}(m^s) + \frac{\partial}{\partial x_i}(m^s u_i) = \frac{\partial}{\partial x_i}\left(D^s \frac{\partial m^s}{\partial x_i}\right) + R^s \tag{3}$$

From this point the local concentration of species at any point inside the system can be calculated and utilized in the calculation of the corrosion rate. To calculate the corrosion rate itself, another equation must be solved, this time at the wall where the corrosion occurs. For this the Butler-Volmer equation, which can be seen below, is implemented as what is known as a boundary condition. Boundary conditions play a big role in CFD simulations as these are the ways in which information is transferred into the system, such as specifying a particular velocity or flow rate at an inlet, or a pressure at an outlet.

$$i_F = i_0 \left(\frac{c}{c_{ref}}\right)^n \left[\exp\left(\frac{2.303\eta}{\beta_a}\right) - \exp\left(\frac{2.303\eta}{\beta_c}\right)\right] \tag{4}$$

This implementation allows for the calculation by the CFD software of the current density of the electrochemical corrosion reaction, which can then be transformed into a corrosion rate.

EXPERIMENTAL PROCEDURE

For the purposes of this project, the current focus is the verification of the hydrodynamics, mass transfer, and electrochemical and chemical reactions in two experimental geometries, the thin channel flow cell (TCFC), and straight pipe flow. In order to verify these parameters in these experimental systems, first literature sources are found which provide either experimental data in these systems, or

correlations which can be used to calculate these parameters based on the conditions tested. When direct comparison with experimental data is to be performed, the experimental systems are designed carefully replicating the significant physical dimensions of the experimental systems used in the literature source. The parameters of the simulation are input to exactly recreate the conditions seen in the experiments being referenced. The relevant simulation results are then compared with the data present in the literature to determine the accuracy of the simulated results. If a correlation is being used for verification, the experimental system is created to satisfy any requirements that the correlation might have to ensure its validity in the simulated system. A range of conditions may then be simulated by changing the simulation parameters such as flow rate and the trend of relevant parameters can be compared against the trend predicted by the correlation. The CFD software used for all simulations is Ansys Fluent™[§].

RESULTS

Thin channel flow Cell (TCFC)

The thin channel flow cell (TCFC) is a piece of experimental equipment commonly used to perform experiments involving high shear stress conditions. The piece of equipment that was used to gather the experimental data which will be later be used for comparison to simulations had a height of 3.57mm, and a length of 3m, although only 200mm was simulated in order to limit the size of the geometry and allow for greater mesh refinement. The simulations were 2-dimensional based on the assumption that the flow across the width of the TCFC would be constant. The mesh generated for the simulations can be seen below in Figure 1.

Figure 1: TCFC mesh.

Inflation was used near the walls of the TCFC to ensure that multiple control volumes inside the mass transfer boundary layer. The inflation utilized a specified first layer thickness and growth rate to gradually increase in size until it matched the bulk mesh size. The refined mesh section can be seen below in Figure 2.

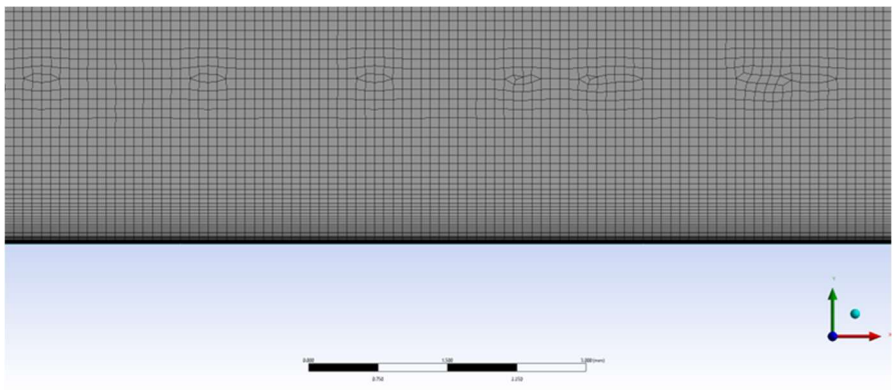

Figure 2: Inflated portion of mesh.

The inlet had a specified value of velocity that was uniform across the boundary, after a certain distance the flow will fully develop into a more realistic flow profile. All data discussed will be taken from regions downstream from the fully developed flow profile. The stable velocity profile can be seen below in Figure 3.

[§] Trade Name

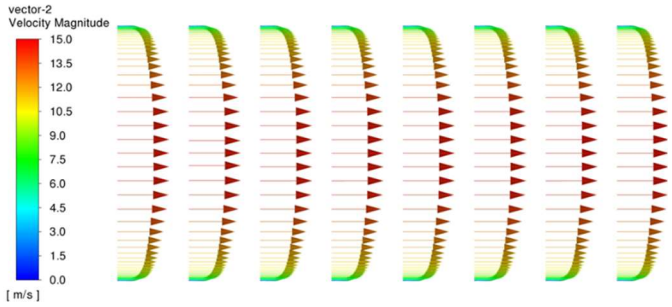

Figure 3: Fully developed flow profile for inlet velocity of 12.9 m/s.

As can be seen in Figure 3 the peak velocity in the flow profile is higher than the inlet velocity, this is due to a combination of the no-slip boundary condition used at the walls and the incompressible nature of the fluid.

Various parameters were checked to ensure the accuracy of the simulations, the first of which was the hydrodynamic characteristics of the flow. Experiments were carried out where the wall shear stress was monitored at various flow velocities, which lead to the development of the equations shown below.[1]

$$\tau = \frac{1}{2}\rho C_f V^2 \tag{5}$$

In this equation τ is the wall shear stress in Pa, ρ is the fluid density in kg/m^3, C_f is the fanning friction factor, and V is the mean flow velocity in m/s. The fanning friction factor for channel flow can be calculated using the Patel correlation.[2]

$$C_f = 0.0376Re^{-1/6} \tag{6}$$

A comparison of the calculated wall shear stress and shear stress obtained from CFD simulations at a variety of flow velocities can be seen below in Figure 4.

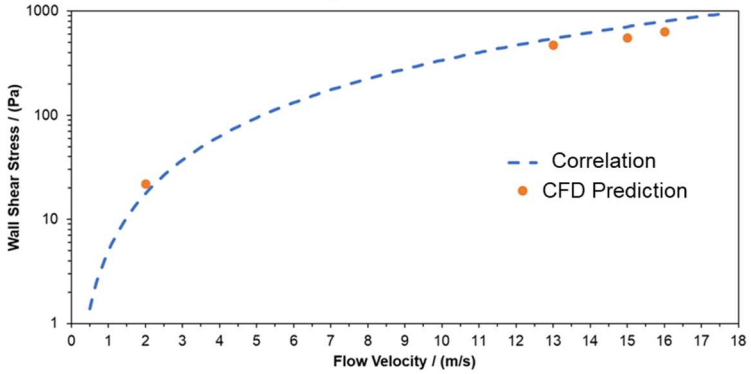

Figure 4: Comparison of theoretical and simulated wall shear stress in TCFC.

Given the good agreement between the CFD simulations and the correlation, it is determined that the CFD simulations are hydrodynamically accurate in this geometry. The next step is to confirm the ability of the CFD software to simulate mass transfer of species in this geometry. Potentiodynamic sweep data was collected in a TCFC and can be seen below in Figure 5.[3]

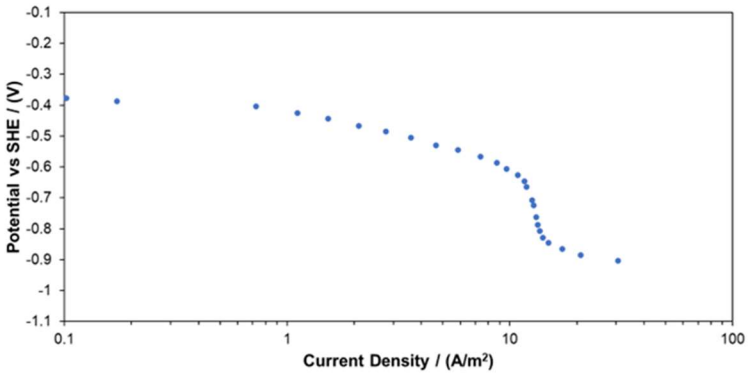

Figure 5: TCFC experimental data during cathodic potentiodynamic sweep at pH 4, V=12.9 m/s, T=30°C.[3]

From the experimental data the mass transfer limited current is seen to be 13.4 A/m^2, and from this information the mass transfer boundary layer can be calculated using the following equation.

$$\frac{D_{ab} n F C_b}{i_{lim}} = \delta_m \tag{7}$$

Where D_{ab} is the diffusivity of H^+ in water, n is the electrical charge of H^+, F is the Faraday constant, C_b is the molar concentration of H^+ in the bulk solution, i_{lim} is the mass transfer limited current density in A/m^2, and δ_m is the mass transfer boundary layer thickness in meters. From this calculation the mass transfer boundary layer thickness is found to be 7 μm. A subsequent CFD simulation of the same conditions where a portion of the TCFC wall is designated as having a concentration of H^+ of 0 M. This represents the conditions in a mass transfer limited scenario where all the H^+ that reaches the surface is consumed, as would happen in a cathodic potentiodynamic sweep. The species concentration profile from the CFD simulation is shown below in Figure 6.

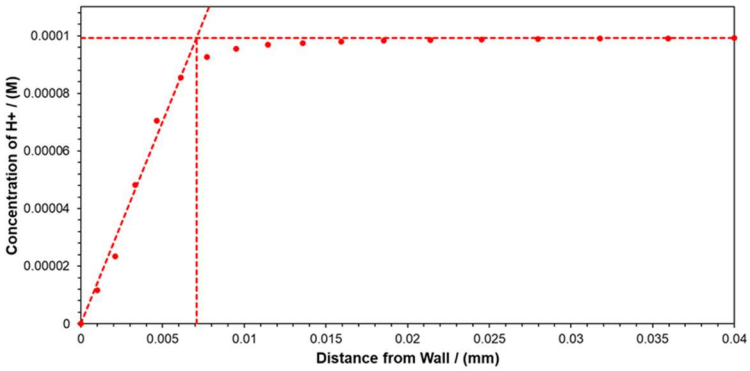

Figure 6: Species concentration profile from CFD simulation of the TCFC and the graphically obtained mass transfer boundary layer thickness.

From the simulated concentration profile and observing the intersection of the two lines shown in Figure 6, the simulated thickness of the mass transfer boundary layer is 7 μm, exactly matching the calculation made based on the experimental data.

The next step was to replace the specified species concentration for H^+ used in the previous simulation with the actual electrochemical reaction that would be occurring and the associated Butler-Volmer parameters.

$$2H^+ + 2e^- \rightleftharpoons H_2 \tag{8}$$

Table 1
Butler-Volmer parameters for hydrogen reduction reaction.

Input Variable	Value
Exchange current density (A/m^2)	0.03
Species concentration (M)	0.0001
Reference mass fraction H^+	0.001
Reaction order	0.5
B_a	0.12
β_c	0.12
Equilibrium potential (V)	0

With the boundary condition changed, a value of the potential is specified on the reactive wall and the current density is calculated by the CFD software. A comparison of the simulated current density values against a potentiodynamic sweep calculated using the Butler-Volmer equation and the previously found mass transfer limiting current is shown below in Figure 7.

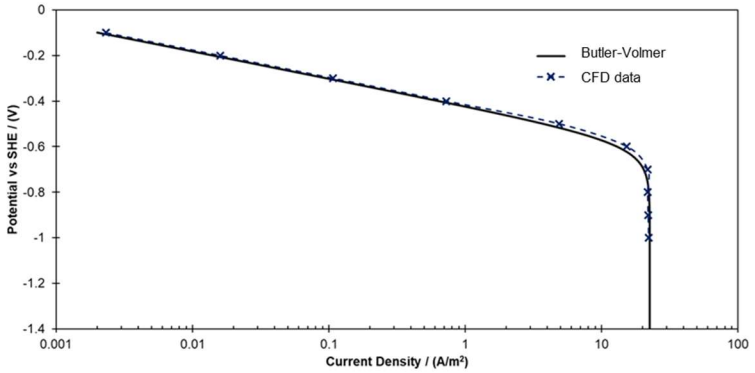

Figure 7: Comparison of potential vs. current density calculated from the Butler-Volmer equation and from CFD simulations.

A good agreement between the simulation results and the calculated values in both the charge transfer controlled region, and the mass transfer controlled region. The next step forward is to include the appropriate anodic reaction to be paired with the cathodic reaction already present, specifically the iron dissolution reaction, as would be seen in a case of strong acid corrosion.

$$Fe \rightleftharpoons Fe^{2+} + 2e^- \tag{9}$$

Table 2
Butler-Volmer parameters for strong acid corrosion simulation.

	Hydrogen Reduction	**Iron Oxidation**
Input Variable	**Value**	
Exchange current density (A/m^2)	0.03	0.005
Species concentration (M)	0.0001, 0.00001	1
Reference mass fraction H^+	1E-07	0.001
Reaction order	0.5	0
β_a	0.12	0.04
β_c	0.12	0.04
Equilibrium potential (V)	-0.24	-0.488

Using the parameters shown in Table 2 as the boundary conditions at the reactive surface representing the metal sample in the TCFC. At the reactive surface the current density will be specified as 0 A/m^2 to

represent a situation where the anodic and cathodic reactions are in equilibrium. A comparison of the corrosion rates predicted by the CFD simulation, and a corrosion rate calculated using the Butler-Volmer equation at two different values of pH can be seen below in Figure 8.

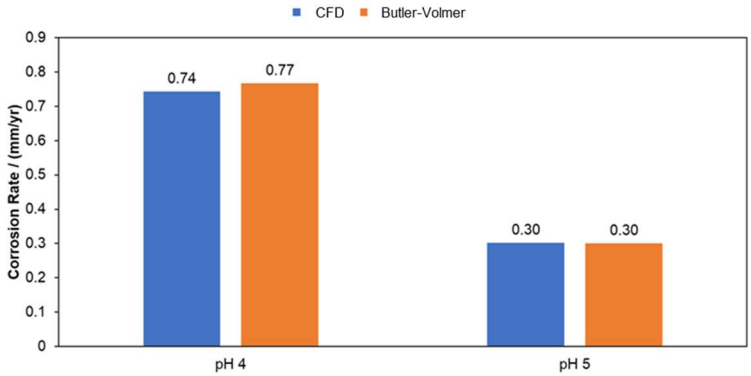

Figure 8: Strong acid corrosion rates at pH 4 and pH 5, calculated from Butler-Volmer equation and CFD simulation.

There is a very good agreement between the simulated and calculated corrosion rates at both pH 4 and pH 5. The next and final step is to include the relevant chemical reactions in the CFD simulations to simulate CO_2 corrosion. For the purposes of this study this will remain a single-phase simulation, the dissolving of gaseous CO_2 into water is not considered here. The relevant chemical reactions are:

$$CO_2 + H_2O \rightleftharpoons H_2CO_3 \tag{10}$$

$$H_2CO_3 \rightleftharpoons HCO_3^- + H^+ \tag{11}$$

$$HCO_3^- \rightleftharpoons CO_3^{2-} + H^+ \tag{12}$$

$$H_2O \rightleftharpoons H^+ + OH^- \tag{13}$$

To include these reactions in the CFD simulations requires the forward and backward rate constants for each reaction at the given conditions, which are given below in Table 3.

Table 3
Rate constants for chemical reaction in CO_2 corrosion simulation.

Reaction	Forward Rate Constant	Backward Rate Constant
CO_2 Hydration	0.0348 s^{-1}	24.5 s^{-1}
H_2CO_3 Dissociation	1.9×10^7 s^{-1}	4.7×10^{10} $M^{-1}s^{-1}$
HCO_3^- Dissociation	181 s^{-1}	3.67×10^{12} $M^{-1}s^{-1}$
H_2O Dissociation	0.00126 Ms^{-1}	1.4×10^{11} $M^{-1}s^{-1}$

The same electrochemical reactions and associated constants used in the strong acid corrosion previously presented are still used. The corrosion rates being used for comparison are data taken from a TCFC at two different values of pH.[3]

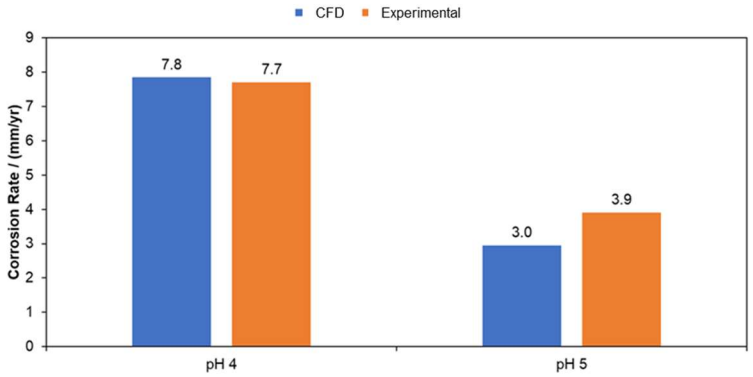

Figure 9: CO_2 corrosion rates at pH 4 and pH 5 from experiments and CFD simulations.

Once again, a good agreement is found between the experimentally obtained corrosion rates and those predicted by the CFD simulations. With this it is concluded that the CFD simulations are able to accurately simulate the hydrodynamics, mass transfer, electrochemical reactions, and chemical reactions present in CO_2 corrosion occurring in a TCFC.

Turbulent pipe flow

Corrosion of oil and gas transmission pipelines is one of the major issues for industries and thus modeling and prediction of corrosion rate in such systems are crucial for these industries in order to mitigate and control the failures due to corrosion. Hence, it was selected as another system for CFD simulation. The geometry and dimension of the simulation for pipe flow is shown in **Error! Reference source not found.**. It is a 2-dimensional simulation in steady state condition and turbulent flow with the velocity of 1 m/s. As boundary conditions for mass transfer simulation, the concentration of the bulk of solution was set at 1 mol/m^3 and, it was zero at the wall of pipe. It should be noted that the results shown for this simulation are related to the fully developed region of the flow.

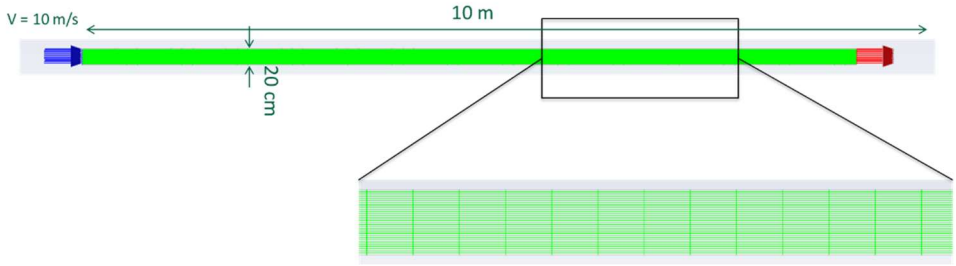

Figure 10: Geometry for simulation of pipe flow.

Figure 11 displays an example of velocity profile for a simulation of pipe flow.

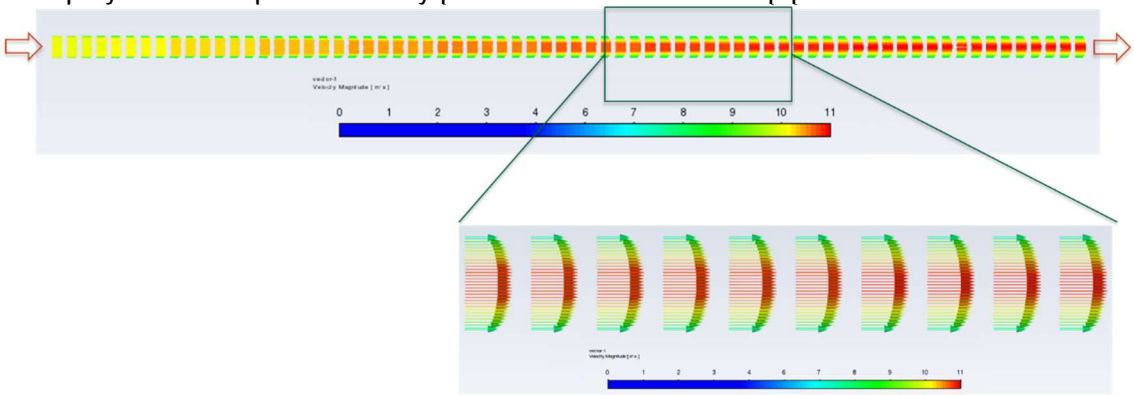

Figure 11: The simulated velocity profile for pipe flow with V = 1 m/s, v= 10^{-6} m^2/s and ρ=1000 kg/m^3.

Same as the previous case, the three parameters can be used for pipe flow to verify the simulated results. The shear stress for pipe flow can be calculated using Colebrook equation for the Darcy friction assuming zero roughness for the pipe's wall.[4,5]

$$C_d = 0.25\left[\log\left(\frac{\frac{\varepsilon}{D_{eq}}}{3.7}+\frac{5.74}{Re^{0.9}}\right)\right]^{-2} = 0.25\left[\log\left(\frac{5.74}{Re^{0.9}}\right)\right]^{-2} = 0.0155 \quad (14)$$

$$\tau_w = \frac{1}{2}\rho C_f V^2 = \frac{1}{8}\rho C_d V^2 = 1.9\ Pa \quad (15)$$

Figure 12 shows the simulated wall shear stress of pipe starting from inlet when the flow is not fully developed to the outlet. As can be observed, the average shear stress in the fully developed region from simulation is close to the theoretical value.

According to the theory of turbulent flow, three different regions should be considered for the flow when plotting non-dimensional velocity versus non-dimensional distance: viscous sublayer, buffer region, and log-law layer[Error! Reference source not found.].[6] Some empirical equations exist in the literatures for viscous sublayer and log-law region as shown on the Figure 13. The buffer region is actually a transition between these two regions. By comparing the simulated results with the theoretical one, a good agreement can be found for viscous sublayer and log-law regions, and some deviations exist in buffer layer.

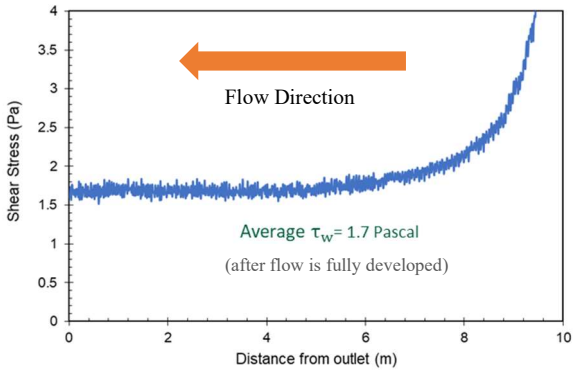

Figure 12: Comparison of simulated and theoretical values for wall shear stress.

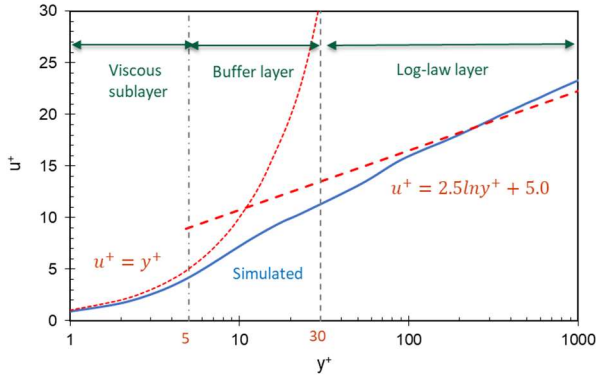

Figure 13. Comparison of simulated and theoretical values for velocity profile for pipe flow.

Finally, for verifying the mass transfer, the mass transfer coefficient has a relationship with the thickness of mass transfer boundary layer according to the literatures. Mass transfer coefficient for the pipe flow can be found from Berger and Hau correlation[7] and then mass transfer boundary layer thickness can be calculated as below.

$$k_{pipe} = 0.0165Re^{0.86}Sc^{0.33}\frac{D}{d_{pipe}} = 1.365 \times 10^{-4} \quad (16)$$

$$\delta_m = \frac{D}{k_{pipe}} = 73\ \mu m \quad (17)$$

Figure 14 shows the simulated concentration profile. As it can be seen, the thickness of mass transfer boundary layer found from simulation agrees very well with the theoretical value.

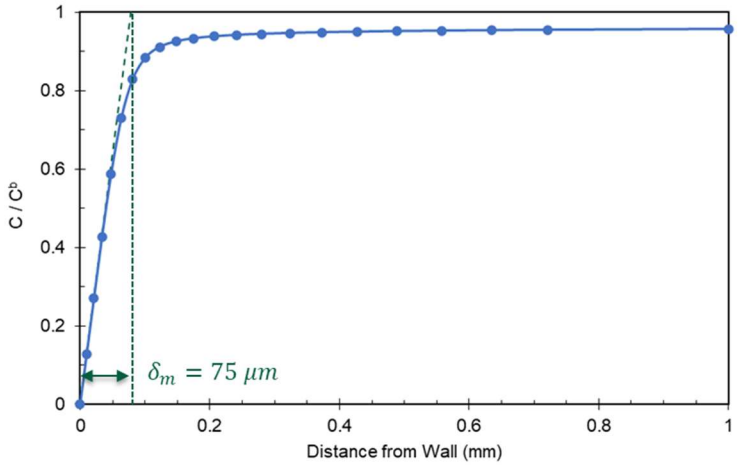

Figure 14: Simulated concentration profile for pipe flow and thickness of mass transfer boundary layer.

For verifying mass transfer, the mass transfer coefficient has a relationship with the thickness of mass transfer boundary layer according to the literatures. Mass transfer coefficient for the pipe flow can be found from Berger and Hau correlation and then mass transfer boundary layer thickness can be calculated as below. It should be mentioned that in this case the velocity of 1 m/s was used as the thickness of the mass transfer boundary layer is larger and therefore more observable at lower velocity.

$$k_{pipe} = 0.0165Re^{0.86}Sc^{0.33}\frac{D}{d_{pipe}} = 1.365 \times 10^{-4} \quad (18)$$

$$\delta_m = \frac{D}{k_{pipe}} = 73\ \mu m \quad (19)$$

Figure 14 shows the simulated concentration profile. As it can be seen, the thickness of mass transfer boundary layer found from simulation agrees very well with the theoretical value.

In order to simulate the corrosion rates, it is necessary to initially establish the boundary conditions for electrochemical reactions including both anodic and cathodic reactions. As discussed in the previous section, the electrochemical reactions involved in the corrosion of mild steel in strong acid solutions are hydrogen ion reduction and iron dissolutions reactions (Reactions (8) and (9)). For this purpose, the boundary condition for the mass transfer at the wall of pipe is given by Butler-Volmer equations as described below:

$$i_F = i_0\left(\frac{c}{c^{ref}}\right)^n\left[\exp\left(\frac{2.303(E-E_{rev})}{\beta_a}\right) - \exp\left(\frac{2.303(E-E_{rev})}{\beta_c}\right)\right] \quad (20)$$

For the simulation of corrosion rates in strong acid solutions for this study, the values of the parameters used in Butler-Volmer equation are listed in Table 4.

Table 4
Butler-Volmer parameters for strong acid corrosion simulation.

Parameter	Hydrogen ion Reduction	Iron Oxidation
Exchange current density (A/m^2)	0.037	1
Species concentration (M)	0.001, 0.0001, 0.00001	-
Reference mass fraction H^+	1E-07	1E-07
Reaction order	1	0
β_a	0.12	0.04
β_c	0.12	0.04
Equilibrium potential (V)	-0.24	-0.488

In order to verify the simulation, the results were compared with the mathematical calculation of corrosion rates from Butler-Volmer equation. The comparison of corrosion rates as well as corrosion potential between CFD simulation and mathematical calculations in different pH values are shown in Figure 15 and Figure 16.

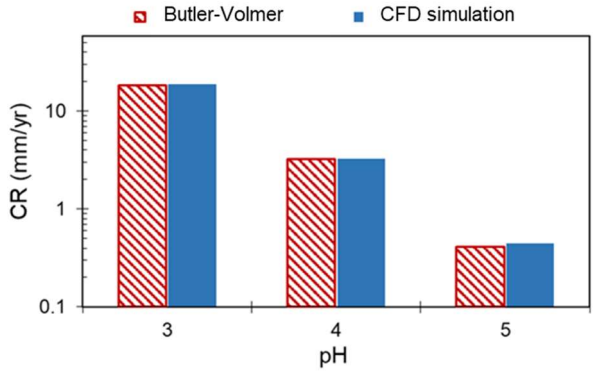

Figure 15. Comparison of simulated and calculated results for corrosion rate at various pH values.

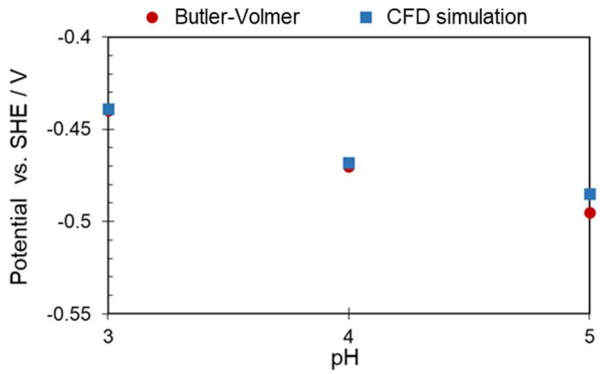

Figure 16. Comparison of simulated and calculated results for corrosion potential at various pH values.

A very good agreement can be found between the simulated and calculated results for both cases of corrosion rate and corrosion potential. In the final step, the corrosion rate was simulated in CO_2 solutions. To simulate CO_2 corrosion, similar to what was discussed for the case of TCFC, four homogenous chemical reactions (Reactions (10) – (13)) were added which incorporate the hydration of CO_2, and subsequent dissociation reactions that provide an additional source of H^+ ions to be used in

the corrosion reaction. The rate constants for these four chemical reactions were also already shown in **Error! Reference source not found.**. It should be considered that the electrochemical reactions involved in CO_2 corrosion are still the same cathodic and anodic reactions with the same values shown in **Error! Reference source not found.**. For validating the simulation results, the data were compared with the simulations from FREECORP** software which is a free online corrosion prediction model. **Error! Reference source not found.** compares the simulation that was performed using CFD software with that obtained using corrosion prediction software at various partial pressure of CO_2.

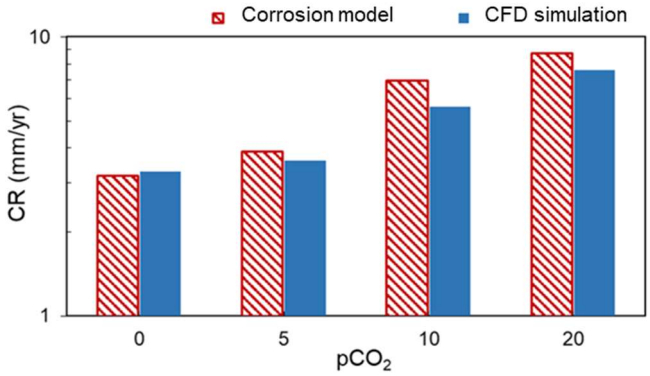

Figure 17: Comparison between CFD simulations and the corrosion prediction model simulations for various partial pressure of CO_2 at pH 4.

As can be observed from the figure, the corrosion rate increased by the increase of the partial pressure of CO_2, due to the buffering effect originating from contribution of homogenous chemical reactions. Also, simulation using CFD software was able to capture the effect of CO_2 through homogenous chemical reactions, and successfully predict the increase of corrosion rates. To investigate the effect of various pH values on the corrosion of mild steel in CO_2 environments, the simulation was performed at two pH values as well as different partial pressure of CO_2, as represented in Figure 18 and Figure 19.

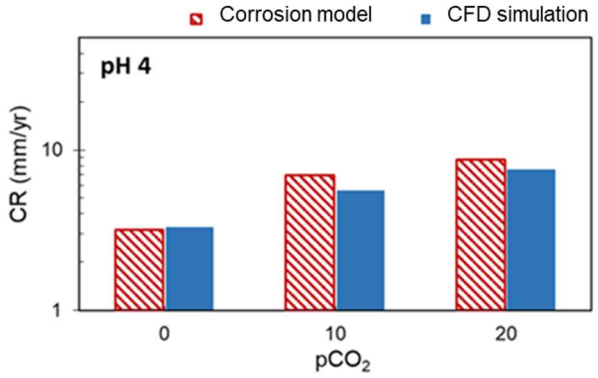

Figure 18: Comparison between CFD simulations and the corrosion prediction model simulations for various partial pressures of CO_2 at pH 4.

** Trade Name

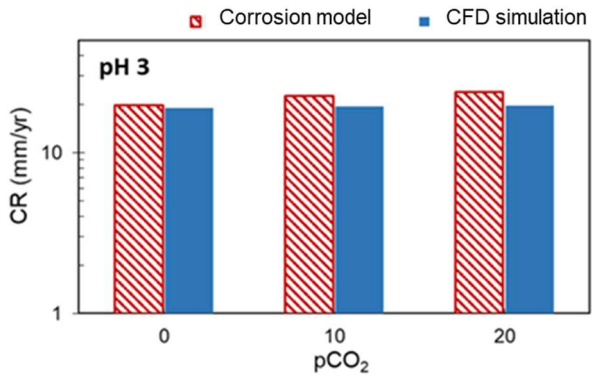

Figure 19: Comparison between CFD simulations and the corrosion prediction model simulations for various partial pressures of CO_2 pH 3.

The results show that the effect of partial pressure of CO_2 is stronger at pH 3 compared with that at pH 4. The reason might be that the corrosion rate at pH 3 is very high and mostly charge transfer controlled, and thus buffering effect has slight impact on the corrosion current. In general, good agreement was obtained between the CFD simulation and the corrosion prediction model simulations in different environmental conditions. Therefore, we can conclude that the corrosion of mild steel in strong acidic solutions as well weak acid solutions was successfully simulated using the CFD software.

CONCLUSIONS

In both the TCFC and pipe geometries, the hydrodynamics, mass transfer, electrochemical and chemical reactions involved in both strong acid and CO_2 corrosion were accurately simulated using CFD software. The accuracy of the simulations was verified using experimental data and correlations and showed good agreement in all areas.

ACKNOWLEDGEMENTS

The author would like to thank the following companies for their financial support:
Ansys, Baker Hughes, ChampionX LLC, Chevron Energy Technology, ConocoPhillips, ExxonMobil, M-I SWACO (Schlumberger), Multi-Chem (Halliburton), Occidental Oil Company, Pertamina, Saudi Aramco, Shell Global Solutions and TotalEnergies.

REFERENCES

(1) Li, W.; Pots, B. F. M.; Brown, B.; Kee, K. E.; Nesic, S. A Direct Measurement of Wall Shear Stress in Multiphase Flow—Is It an Important Parameter in CO2 Corrosion of Carbon Steel Pipelines? *Corros. Sci.* **2016**, *110*, 35–45. https://doi.org/10.1016/j.corsci.2016.04.008.
(2) Patel, V. C.; Head, M. R. Some Observations on Skin Friction and Velocity Profiles in Fully Developed Pipe and Channel Flows. *J. Fluid Mech.* **1969**, *38* (1), 181–201. https://doi.org/10.1017/S0022112069000115.
(3) Kahyarian, A. Mechanism and Prediction of Mild Steel Corrosion in Aqueous Solutions Containing Carboxylic Acids, Carbon Dioxide, and Hydrogen Sulfide, Ohio University, Athens Ohio, 2018.
(4) Swamee Prabhata K.; Jain Akalank K. Explicit Equations for Pipe-Flow Problems. *J. Hydraul. Div.* **1976**, *102* (5), 657–664. https://doi.org/10.1061/JYCEAJ.0004542.
(5) Colebrook, C. F.; White, C. M.; Taylor, G. I. Experiments with Fluid Friction in Roughened Pipes. *Proc. R. Soc. Lond. Ser. - Math. Phys. Sci.* **1997**, *161* (906), 367–381. https://doi.org/10.1098/rspa.1937.0150.
(6) Cengel, Y.; Cimbala, J. *Fluid Mechanics: Fundamentals and Applications*, 4th ed.; McGraw-Hill, 2014.

(7) Berger, F. P.; Hau, K.-F. F.-L. Mass Transfer in Turbulent Pipe Flow Measured by the Electrochemical Method. *Int. J. Heat Mass Transf.* **1977**, *20* (11), 1185–1194. https://doi.org/10.1016/0017-9310(77)90127-2.